A Mathematical Model of the Coupled Fluid Mechanics and Chemical Kinetics in a Chemical Vapor Deposition Reactor

Michael E. Coltrin

Sandia National Laboratories, Laser and Atomic Physics Division, Albuquerque, New Mexico 87185

Robert J. Kee

Sandia National Laboratories, Applied Mathematics Division, Livermore, California 94550

James A. Miller

Sandia National Laboratories, Combustion Chemistry Division, Livermore, California 94550

ABSTRACT

We describe a numerical model of the coupled gas-phase hydrodynamics and chemical kinetics in a silicon chemical vapor deposition (CVD) reactor. The model, which includes a 20-step elementary reaction mechanism for the thermal decomposition of silane, predicts gas-phase temperature, velocity, and chemical species concentration profiles. It also predicts silicon deposition rates at the heated reactor wall as a function of susceptor temperature, carrier gas, pressure, and flow velocity. We find excellent agreement with experimental deposition rates, with no adjustment of parameters. The model indicates that gas-phase chemical kinetic processes are important in describing silicon CVD.

The chemical vapor deposition (CVD) of solid materials is an important method for producing solid films with high purity and uniformity. Some important applications of CVD include the manufacture of microelectronic devices and silicon solar cells. Even though CVD has widespread use, a fundamental understanding of the interplay among its constituent elements is missing. A unified theoretical picture of CVD requires input from the fields of gas-phase chemical kinetics, fluid mechanics, surface chemistry, and materials science.

In this paper we describe a two-dimensional mathematical model of the coupled gas-phase kinetics and hydrodynamics in a laminar-flow chemical vapor deposition reactor. Specifically, we have studied a reactor in which silicon is deposited as the result of the thermal decomposition of silane. This system was chosen for its relative simplicity and its importance to the microelectronics industry. Nevertheless, our model is quite general, and thus can be applied to other CVD systems if the appropriate gas-phase reaction mechanisms are known.

Our model couples the chemical rate equations with the boundary layer equations describing the hydrodynamics, producing a system of parabolic partial differential equations which are solved numerically. We employ a relatively simple reaction mechanism to describe the inhomogeneous gas-surface chemistry. Ultimately we should include a more detailed model of the surface chemistry, but presently we are primarily interested in a quantitative description of the gas phase. Moreover, as we discuss later, this gas-phase model alone is very successful in describing CVD experimental observables. Our treatment of the gas phase is greatly aided by our earlier work on modeling combustion chemistry (1, 2). Also, our modeling is performed in conjunction with experimental measurements of chemical species concentrations in the gas phase (3).

Our principal purpose in this paper is to present a complete description of the mathematical and numerical formalism of the model. There have been many other theoretical approaches to modeling CVD, however, most of these models have not considered the possibility of gas-phase chemistry. The present model is the most detailed model of the gas phase in CVD to date.

Below we present details of the model, including the set of governing partial differential equations, the reaction mechanism describing SiH_4 pyrolysis, and the numerical solution method. We also present computed temperature, velocity, and chemical species concentration profiles. We compare predicted deposition rates with experimental results.

Key words: CVD, growth, kinetics, transport.

Model Formulation

Transport equations.—We assume in this work that the boundary layer approximations are valid. That is, the Navier-Stokes equations can be reduced to a system of parabolic partial differential equations describing the conservation of mass, momentum, energy, and species composition. The approximation relies on the existence of a principal flow direction in which convective transport is dominant and diffusive effects are negligible. In this approach the pressure is impressed on the flow by the boundary conditions and is uniform in the cross-stream direction. The imposition of pressure replaces the cross-flow momentum equation entirely.

After making the boundary layer approximations, we use the Von Mises transformation (4) to cast the equations in a form in which the stream function replaces the radial coordinate as an independent variable. This transformation eliminates the mass conservation equation, replacing it with an integral. Additionally, it eliminates any explicit reference to the cross-stream convective terms in the resulting system of equations.

The system of equations which form our model are described as follows

Momentum

$$\rho u \frac{\partial u}{\partial x} + \frac{\partial p}{\partial x} = \rho u \frac{\partial}{\partial \psi}\left(\rho u \mu y^{2\alpha} \frac{\partial u}{\partial \psi}\right) + \rho g \qquad [1]$$

Species

$$\rho u \frac{\partial Y_k}{\partial x} = \dot{\omega}_k W_k - \rho u \frac{\partial}{\partial \psi}\left(y^\alpha \rho Y_k V_{k_y}\right) \quad (k = 1, K) \qquad [2]$$

Energy

$$\rho u c_p \frac{\partial T}{\partial x} = \rho u \frac{\partial}{\partial \psi}\left(\rho u \lambda y^{2\alpha} \frac{\partial T}{\partial \psi}\right) - \sum_{k=1}^{K} \dot{\omega}_k W_k h_k - \rho^2 u y^\alpha \sum_{k=1}^{K} Y_k V_{k_y} c_{pk} \frac{\partial T}{\partial \psi} \qquad [3]$$

State

$$p = \rho \frac{\mathrm{R}}{\overline{W}} T \qquad [4]$$

The diffusion velocity V_{k_y} is given in the new coordinates by

$$V_{k_y} = -\frac{D_k}{X_k} \rho u y^\alpha \frac{\partial X_k}{\partial \psi} \qquad [5]$$

In these equations, the independent variables x and ψ represent the axial coordinate and stream function, re-

spectively. For an axisymmetric flow, the parameter α is 1, and y represents the radius measured from the flow centerline. For $\alpha = 0$ the equations are in planar coordinates. In both cases, the cross-stream coordinate y is a dependent variable and is given in terms of stream function by the following integral

$$\frac{y^{\alpha+1}}{\alpha+1} = \int_0^{\psi} \frac{d\psi'}{\rho u} \quad [6]$$

or, in the differential equation form that we actually use, by

$$\frac{\partial y^{\alpha+1}}{\partial \psi} = \frac{\alpha+1}{\rho u} \quad [7]$$

Other variables are given by: u, the axial fluid velocity; ρ, the mass density; p, the thermodynamic pressure; T, the temperature; Y_k, the mass fraction of the kth species; X_k, the mol fraction of the kth species; W_k, the molecular weight of the kth species; R, the universal gas constant; g, the acceleration of gravity; D_k, the binary diffusion coefficient of the kth species into the mixture; μ, the mixture viscosity; λ, the mixture conductivity; c_p, the specific heat at constant pressure; h_k, the specific enthalpy of the kth species; $\dot{\omega}_k$, the rate of production of the kth species by chemical reaction: $\overline{W}$, the mixture's mean molecular weight.

The transport properties (viscosity, thermal conductivity, and diffusion coefficients) are temperature dependent and are obtained from Lennard-Jones parameters for each of the chemical species using standard techniques (5-8). The specific formulas employed are discussed in detail by Kee and Miller (9).

We compute thermodynamic properties (heat capacities, entropies, and enthalpies) for each of the chemical species from temperature-dependent fits of data [JANAF when available (10)] in the form used by the NASA chemical equilibrium code (11). Thermochemical data were not available for SiH_2, SiH_3, Si_2H_2, Si_2H_3, Si_2H_4, Si_2H_5, and Si_2H_6. For these species we used the results of an extensive set of electronic structure calculations by Binkley (12) to estimate entropies, energies, and harmonic vibrational frequencies. Standard statistical mechanical techniques (13) were used to convert the frequencies and energies to $c_p(T)$, $h(T)$, and $s(T)$, which were then fit to the polynomial form of Gordon and McBride (11). In the code all chemical production rate terms, thermodynamic properties, and equation of state variables are evaluated by appropriate subroutine calls to CHEMKIN (14), a general-purpose package of chemical kinetics Fortran subroutines.

Boundary conditions.—The two different channel types treated here, axisymmetric and planar, each require slightly different boundary condition formulations. In both cases the equations are parabolic, so boundary conditions are specified for u, T, Y_k, y, and p at the boundary $x = 0$. However, since the x coordinate is time-like for purposes of numerical solution algorithms, the boundary conditions at $x = 0$ may be regarded as initial conditions. In equations of this type (differential/algebraic equations), all of the initial conditions are not independent. Once u, T, Y_k, and p are specified at $x = 0$, the cross-stream velocity v follows as an integral of the mass conservation equation. In stream function coordinates, where v has been eliminated as a variable, it follows that the physical coordinate y must be consistent with the other initial conditions.

The channel walls (or an axis of symmetry and a wall) define the flow boundaries. In stream function coordinates, the walls correspond to streamlines, or lines of constant stream function. By definition, flow is tangent to streamlines; thus, no flow crosses a wall (or axis of symmetry). The boundary condition, corresponding to either the lower wall or the axis of symmetry, is applied at $\psi = 0$. The other boundary condition is applied at ψ_0, where ψ_0 is determined from Eq. [6] when ψ and u are evaluated at the initial conditions, and an initial mesh in y is specified.

For axisymmetric problems, an axis of symmetry is specified at $\psi = 0$ by

$$\frac{\partial u}{\partial \psi} = \frac{\partial T}{\partial \psi} = \frac{\partial Y_k}{\partial \psi} = 0 \quad [8]$$

In addition, we specify that $y = 0$ at $\psi = 0$.

On solid walls we specify the no-slip boundary, $u = 0$. In some cases we specify T itself, while in others we specify a heat flux, *i.e.*, a temperature gradient. Zero gradients are imposed for the mass fractions of species that do not react at walls (implying no mass flux to the wall). For species that react at the wall, the boundary conditions are more complex, and are discussed below.

Chemical reactions at solid surfaces.—The boundary conditions on chemical species concentrations at a heated surface depend on the extent to which each species undergoes surface reactions. Some species react at the heated surface, depositing silicon. In this model we consider two types of deposition reactions, depending on whether the species is a saturated or unsaturated compound.

Because of the reactive nature of unsaturated chemical species, we assume that they react with the solid surface with unit probability and release molecular hydrogen; in this model these species are SiH, SiH_2, SiH_3, Si_2H_2, Si_2H_3, Si_2H_4, and Si_2H_5. Species that react with unit probability on the surface cannot exist there (because they react instantaneously), and thus the boundary condition for those species is given by

$$Y_{SiH} = Y_{SiH_2} = Y_{SiH_3} = Y_{Si_2H_2} = Y_{Si_2H_3} = Y_{Si_2H_4} = Y_{Si_2H_5} = 0 \quad [9]$$

Results of our model are relatively insensitive to this boundary condition. For example, changing the assumed surface-reaction probability from 1 to 0.8 changes the predicted deposition rate by 5% or less.

We assume that the species H, Si_2H_6, and inert carrier gases do not react at the surface. These species have zero flux to the surface, and thus we enforce the following boundary conditions

$$V_{yH} = V_{ySi_2H_6} = 0 \quad [10]$$

We use the empirical silane surface reaction coefficient of Farrow (15) to describe the deposition due to SiH_4 reacting at the surface. The fraction of silane molecules that decompose upon collision with a heated surface is given by

$$\gamma = 5.45 \exp(-8556/T) \quad [11]$$

However, only a fraction of the silane that decomposes at the surface leads to the formation of solid silicon. According to Farrow's data, this fraction is given by

$$\sigma = 7.6 \times 10^{-3} \exp(3535/T) \quad [12]$$

We assume, as did Farrow, that the rest of the silicon formed by the surface decomposition diffuses away from the surface as gas-phase silicon atoms.

The surface-decomposition fraction (γ) is incorporated into the model as a boundary condition on the SiH_4 concentration. This reaction coefficient is defined as the fraction of the silane flux into the boundary which is decomposed. At steady state, the net flux (incoming minus outgoing flux) at the boundary is equal to the surface reaction rate. The ratio of the flux that would be present for a fractional reaction probability to the flux for a unit reaction probability equals the fraction of the flux which is decomposed. In other words, this ratio is equal to γ of Eq. [11], and the boundary condition derived from this relationship is

$$(V_{ySiH_4}) = \gamma(J_{ySiH_4})_{\gamma=1} \quad [13]$$

The notation $(J_{ySiH_4})_{\gamma=1}$ refers to flux which would exist if the concentration of SiH_4 were zero on the boundary, *i.e.*, unit reaction probability.

From Eq. [12] we can calculate the amount of gas-phase Si atoms formed as a fraction $(1 - \sigma)$ of the silane decomposed at the surface. Equation [14] determines the flux of Si(g) away from the surface

$$\frac{-V_{ySi}Y_{Si}}{W_{Si}} = (1-\sigma)\frac{V_{ySiH_4}Y_{SiH_4}}{W_{SiH_4}} \quad [14]$$

We now need a relationship between the flux of reactive species into the surface and the flux of hydrogen away from the surface. The hydrogen that was initially tied up in silicon containing species is released when the silicon is deposited. In our model the hydrogen atom flux to the surface is balanced by a flux of molecular hydrogen from the surface. (These incoming hydrogen atoms are contained in the surface reacting species.) This relationship is stated in the following boundary condition

$$-\frac{V_{y\mathrm{H_2}}Y_{\mathrm{H_2}}}{W_{\mathrm{H_2}}} = \frac{V_{y\mathrm{SiH}}Y_{\mathrm{SiH}}}{2W_{\mathrm{SiH}}} + \frac{V_{y\mathrm{SiH_2}}Y_{\mathrm{SiH_2}}}{W_{\mathrm{SiH_2}}} + \frac{3V_{y\mathrm{SiH_3}}Y_{\mathrm{SiH_3}}}{2W_{\mathrm{SiH_3}}} + \frac{2V_{y\mathrm{SiH_4}}Y_{\mathrm{SiH_4}}}{W_{\mathrm{SiH_4}}} + \frac{V_{y\mathrm{Si_2H_2}}Y_{\mathrm{Si_2H_2}}}{W_{\mathrm{Si_2H_2}}} + \frac{3V_{y\mathrm{Si_2H_3}}Y_{\mathrm{Si_2H_3}}}{2W_{\mathrm{Si_2H_3}}} + \frac{2V_{y\mathrm{Si_2H_4}}Y_{\mathrm{Si_2H_4}}}{W_{\mathrm{Si_2H_4}}} + \frac{5V_{y\mathrm{Si_2H_5}}Y_{\mathrm{Si_2H_5}}}{2W_{\mathrm{Si_2H_5}}} \quad [15]$$

The cross-flow velocity must vanish at both the upper and lower boundaries of a channel, *i.e.*, $v = 0$. In stream function coordinates this is accomplished by requiring that the physical coordinate y is zero at the lower surface (or axis of symmetry), and that y equals the channel width (or radius) at the upper streamline ψ_0. However, since the equation for y [7] is first order, we normally could not require two boundary conditions. We overcome this restriction by retaining the pressure as dependent variable. The extra boundary condition thus allows us to obtain the unique pressure function $p(x)$ (subject to the given value of p at $x = 0$), which is consistent with having two walls (or one wall and an axis of symmetry) in the problem. During the course of the solution we must determine the $p(x)$ which allows the two boundary conditions on $y(\psi)$ to be satisfied simultaneously. In other words, the pressure drop is computed to balance the shear forces exerted by the walls on the fluid.

Chemical reaction mechanism.—The kinetics of SiH_4 thermal decomposition has been the subject of a number of studies (16-20). The reaction mechanism for silane decomposition employed in this work is given in Table I. A further discussion of the reaction mechanism is presented elsewhere (21). Its development was in essentially two stages. First, a large system of 120 elementary reactions was constructed. Using that mechanism, we performed extensive sensitivity analysis (without any transport effects). From this analysis we determined that silane pyrolysis under conditions of interest could be described as a constrained equilibrium process (22). That is, the time evolution of all the species concentrations is determined strictly by the initial silane dissociation step, whose rate coefficient has been experimentally determined (16). Subsequent radical-molecule and radical-radical reactions simply act to shuffle the intermediate species concentrations to their constrained equilibrium values. Therefore, in the interests of simplicity in the boundary layer computations, we reduced the reaction mechanism to the current 20-step mechanism. Over the range of interest this reduced reaction set reproduces the essential features of the full mechanism, *i.e.*, the initiation step is correct and the constrained equilibrium character is preserved.

Table I. Reaction mechanism

Reaction number	Reaction	A[a]	E_a[a]	Reference
R1	$SiH_4 \rightarrow SiH_2 + H_2$	5.00E12	52.2	(16)
R2	$SiH_4 \rightarrow SiH_3 + H$	3.69E15	93.	(17, 21)
R3	$SiH_4 + SiH_2 \rightarrow Si_2H_6$	5.01E12	1.29	(18)
R4	$Si_2H_4 + H_2 \rightarrow SiH_4 + SiH_2$	6.22E16	2.	(21)
R5	$SiH_4 + H \rightarrow SiH_3 + H_2$	1.04E14	2.5	(19, 20)
R6	$SiH_4 + SiH_3 \rightarrow Si_2H_5 + H_2$	1.77E12	4.4	(21)
R7	$SiH_4 + SiH \rightarrow Si_2H_3 + SiH_2$	1.38E12	11.2	(21)
R8	$SiH_4 + SiH \rightarrow Si_2H_5$	2.93E12	2.	(21)
R9	$SiH_4 + Si \rightarrow 2SiH_2$	9.31E12	2.	(21)
R10	$Si + H_2 \rightarrow SiH_2$	1.15E14	2.	(21)
R11	$SiH_2 + SiH \rightarrow Si_2H_3$	1.26E13	2.	(21)
R12	$SiH_2 + Si \rightarrow Si_2H_2$	7.24E12	2.	(21)
R13	$SiH_2 + Si_3 \rightarrow Si_2H_2 + Si_2$	1.43E11	18.8	(21)
R14	$H_2 + Si_2H_2 \rightarrow Si_2H_4$	2.45E14	2.	(21)
R15	$H_2 + Si_2H_4 \rightarrow Si_2H_6$	9.31E12	2.	(21)
R16	$H_2 + SiH \rightarrow SiH_3$	3.45E13	2.	(21)
R17	$H_2 + Si_2 \rightarrow Si_2H_2$	1.54E13	2.	(21)
R18	$H_2 + Si_2H_3 \rightarrow Si_2H_5$	2.96E13	2.	(21)
R19	$Si_2H_2 + H \rightarrow Si_2H_3$	8.63E14	2.	(21)
R20	$Si + Si_3 \rightarrow 2Si_2$	2.06E12	24.1	(21)

[a] Arrhenius parameters for the rate constants in the form $k_i = A_i \exp(-E_a/RT)$. The units of A_i depend on the reaction order, but are given in terms of mols, cubic centimeters, and seconds. E_a is in kcal/mol.

As part of the analysis of the reaction mechanism we did a formal sensitivity analysis (23), and determined small sensitivities for all rate constants except the initiation step. In addition, in the boundary layer calculations, we did a series of tests in which each of the rate constants of the secondary reactions (R2-R20) were arbitrarily increased and decreased by a factor of 10, and we found that the predicted deposition rates were unaffected. On the other hand, similar tests show a measurable sensitivity to the initiation step. This sensitivity, of course, depends on the particular temperature and flow conditions.

Numerical method.—Method-of-lines formulation.—Our general approach is that of the method-of-lines. After discretization of the spatial derivatives, numerical solution of the resulting system of differential/algebraic equations (DAE's) is accomplished with a code developed by Petzold (24) called DASSL. DASSL solves the equations in a marching fashion, starting from the inflow boundary ($x = 0$) and going toward the outflow boundary. The code implements a variable-order, variable-step algorithm based on the backward differentiation formula (BDF) methods (25). These are stable methods that are particularly well suited for solution of the stiff equations that occur in chemical kinetic models. The DASSL code chooses a sequence of time steps (actually x-coordinate steps) such that the local truncation error in the marching direction is controlled to within a prespecified error tolerance. The general approach in using DASSL is to write a residual function $g(t, y, y')$ at each mesh point, which is zero when the equations are satisfied. DASSL iterates on the solution at each time step until the approximate solution y and y' are sufficiently accurate and so g is zero.

We make the distinction here between standard form ordinary differential equations (ODE's) which are written as $y' = f(t, y)$, and DAE's, which are written in the more general form $g(t, y, y') = 0$. For our purpose, systems of DAE's are distinguished from ordinary systems of parabolic equations by (*i*) an inability to isolate one time-like derivative per equation (the x derivatives in the boundary layer problem), and/or (*ii*) coupled equations which have no time-like derivatives. The former situation occurs in our equations when both $\partial u/\partial x$ and $\partial p/\partial x$ appear in the momentum equation. The latter situation occurs in the equations defining the spatial coordinate y in terms of the stream function via Eq. [7], and in specifying a uniform pressure across the channel. The boundary conditions in the y-coordinate are also regarded as algebraic equations.

Approximation of the spatial derivatives is accomplished by finite difference representations on a fixed grid in the stream function. In the momentum, species, and energy equations, we approximate the second derivatives with conventional central difference formulas as

$$\frac{\partial}{\partial\psi}\left(a\frac{\partial f}{\partial\psi}\right) \approx \left(\frac{2}{\psi_{j+1}-\psi_{j-1}}\right)\left[a_{j+1/2}\left(\frac{f_{j+1}-f_j}{\psi_{j+1}-\psi_j}\right) - a_{j-1/2}\left(\frac{f_j-f_{j-1}}{\psi_j-\psi_{j-1}}\right)\right] \quad [16]$$

where the subscript j denotes the jth grid point. We approximate the first derivatives, as needed in Eq. [3], by central differences as

$$\frac{\partial T}{\partial\psi} \approx \frac{T_{j+1}-T_{j-1}}{\psi_{j+1}-\psi_{j-1}} \quad [17]$$

We evaluate terms with no derivatives, such as the chemical production rate in Eq. [2], using the conditions existing at ψ_j. Likewise, the coefficients of derivatives, such as ρu in Eq. [1], are also evaluated at ψ_j.

Integral conditions such as Eq. [6] (or, equivalently, first-order ODE's) are differenced according to the trapezoidal rule as

$$\frac{y_j^{\alpha+1} - y_{j-1}^{\alpha+1}}{\psi_j - \psi_{j-1}} = (\alpha + 1)\frac{2}{\rho_j u_j + \rho_{j-1}u_{j-1}} \quad [18]$$

It is important to represent the integral equations as first-order differential equations and include the variables such as $y^{\alpha+1}$ in the dependent variable vector. The reason for this choice is associated with the structure of the Jacobian matrix which is needed ultimately to solve the problem. When Eq. [18] is used, the number of dependent variables increases, but the Jacobian remains banded (a very desirable feature). On the other hand, if $y^{\alpha+1}$ is considered as a coefficient in the transport equations as defined by the integral Eq. [6], then the Jacobian loses its banded property and the required computer storage increases enormously.

Boundary conditions.—We treat the boundary mesh points the same way logically as we do the interior points. That is, we consider each dependent variable as an unknown on the boundaries and solve a system of equations to determine its value. Since the boundary equations usually do not involve marching derivatives, using such a formalism requires that the full system be solved as a system of DAE's. The procedure may appear inefficient when the boundary values are known exactly and therefore need not be considered as variables. However, its advantage is that all boundary conditions, regardless of complications (*e.g.*, surface reactions involving many species), are treated in the same manner logically. Thus the boundary conditions of a problem can change without changing the logical structure of the dependent variable vector and the Jacobian. Changing from one set of boundary conditions to a completely different set requires very little programming effort. Moreover, with this formalism, boundary conditions on one equation may be functions of variables which would nominally be associated with another equation. For example, a surface reaction boundary condition typically involves several species concentrations and temperature.

As a final note on the numerical method, we discuss application of the uniform pressure condition. Since it is uniform, we could consider the pressure as a single component in the dependent variable vector. However, since the pressure appears in each equation at each mesh point (either directly as $\partial p/\partial x$ or indirectly in transport property evaluations), using only one variable is undesirable because so doing destroys the block tridiagonal Jacobian structure. We therefore consider the pressure to be an unknown at each mesh point, and solve an equation that forces the pressure at adjacent mesh points to be equal, *i.e.*, $dp/d\psi = 0$. Although we increase the number of dependent variables, we retain the desired Jacobian structure. The finite difference equation at the mesh points states simply that pressure at adjacent nodes is equal

$$p_j - p_{j+1} = 0 \quad [19]$$

The boundary condition applied to Eq. [19] is that y at the outer channel wall is equal to the physical coordinate at the wall. In other words, there is no explicit boundary condition on pressure per se, but the needed boundary condition on y is used implicitly. Note that unlike Eq. [18], which involves nodes j and $j - 1$, Eq. [19] involves nodes j and $j + 1$. This indexing is needed to maintain the block tridiagonal Jacobian structure. We evaluate Eq. [18] at the inner boundary and Eq. [19] at the outer boundary; therefore they are both part of the boundary condition specification at their respective boundaries.

Predictions of Model

The computer model predicts a large number of experimentally observable quantities in the CVD cell; these are discussed individually below. These predictions fall into three broad categories: gas-flow properties, chemical species concentration fields, and deposition rates. Calculated fluid flow quantities include temperature fields, flow streamlines, and velocity fields; these are plotted in Fig. 1.

Two dimensional temperature contours predicted by the model are given in Fig. 1a for a typical run. The incoming gas temperature, at the left of Fig. 1a, is taken as 300 K. The gas is heated from contact with the hot lower surface, causing temperature gradients above the susceptor. Temperature profiles predicted depend on susceptor temperature, flow rate, and carrier gas. As an example, in Fig. 2 we compare temperature profiles under different flow conditions at a fixed susceptor temperature and distance along the susceptor.

Temperature profiles in Fig. 2 for He and H_2 are almost identical because their transport properties are very similar. However, gas-phase chemistry rates and deposition rates are dramatically different in these two carrier gases. The effect of flow velocity on temperature profiles is illustrated in Fig. 2. Increasing the He flow rate by a factor

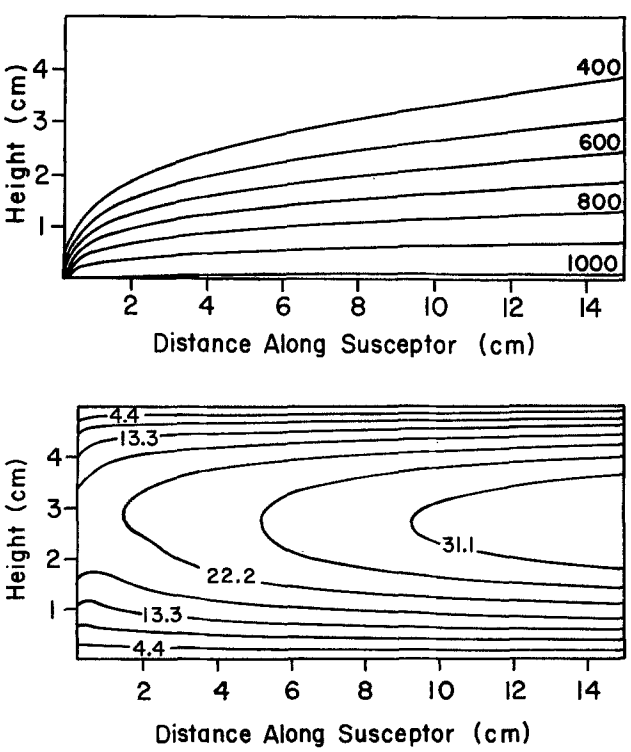

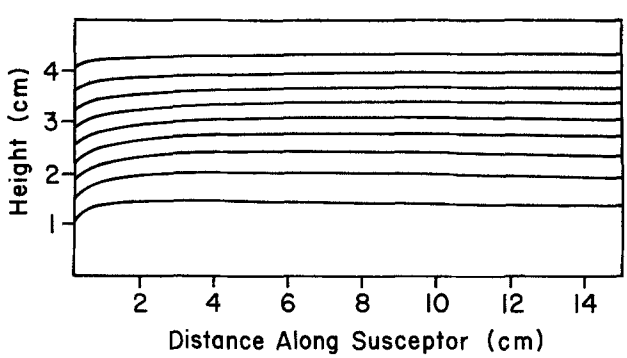

Fig. 1. Fluid flow properties predicted by the numerical model for a typical CVD calculation. Input conditions: susceptor temperature = 1018 K, inlet gas temperature = 300 K, average gas velocity = 15.3 cm/s, 0.6 torr SiH_4 in 640 torr He. A, upper left: temperature contours, labeled in Kelvin. B, upper right: flow streamlines. C, left: gas velocity contours, labeled in cm/s.

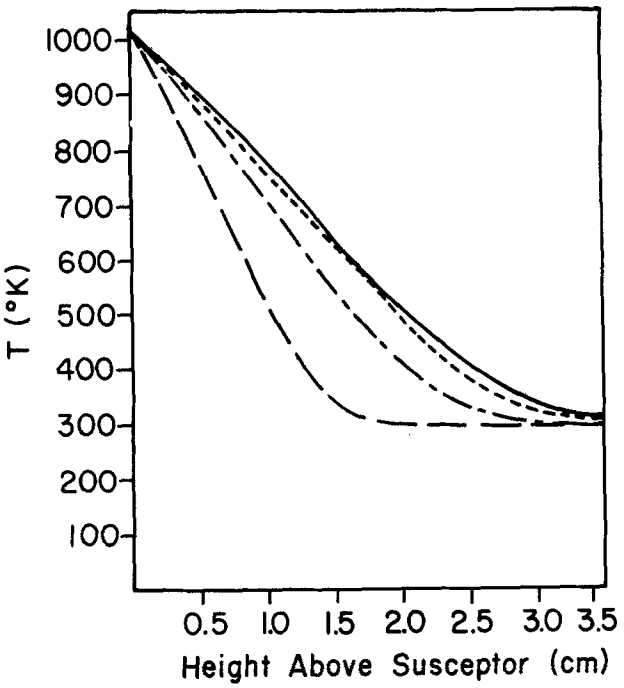

Fig. 2. Temperature profiles as a function of height above the susceptor, calculated for different carrier gases and initial velocities. Input conditions: susceptor temperature = 1018 K, 0.6 torr SiH_4 in 640 torr carrier gas. Profiles are calculated at 4.5 cm from the leading edge of the susceptor. Carrier gases and average velocities are as follows, N_2: 15.3 cm/s (dashed curve). H_2: 15.3 cm/s (dotted curve). He: 15.3 cm/s (solid curve). He: 30.6 cm/s (alternating dash-dot curve).

of two creates a sharper temperature gradient; the gas has shorter residence time in the heated region, and therefore higher temperatures cannot extend as far into the gas. Temperature profiles in N_2 carrier are much steeper than in He because nitrogen has a much smaller thermal conductivity. Although N_2 and He are both inert CVD carrier gases, they are not completely interchangeable. The dissimilar temperature profiles will make the extent of gas-phase reactions much different.

Flow streamlines predicted by the model are plotted in Fig. 1b. The streamlines are forced away from the susceptor at its leading edge. The physical explanation for this phenomena is simple. When the gas enters the heated region it expands. Because, by definition, the volume flow rate between two streamlines is constant, the y position of the lower streamline must increase. Most of the expansion of the gas takes place at the leading edge of the susceptor, so the streamlines remain relatively horizontal downstream. Figure 1c shows velocity contours for a typical calculation. We assume the velocity profile at the inlet to be fully developed, *i.e.*, parabolic. The velocity profile remains roughly parabolic further downstream, but the maximum velocity increases due to expansion of the gas.

Chemical species concentrations result from gas-phase chemical reactions in the fluid-flow field. Because the reactions are very temperature sensitive, they exhibit a 2-D spatial variation with the gas-phase temperature. The resulting concentration profiles are thus a sensitive function of susceptor temperature, flow velocity, and carrier gas. Thermal decomposition of silane is rapid in the gas phase close to the hot susceptor. The model predicts the SiH_4 concentration profiles as a function of distance along the suceptor, as illustrated in Fig. 3. At the inlet there is a uniform concentration of room temperature SiH_4 above the susceptor. Downstream, chemical reactions, primarily reaction R1, deplete silane in the gas phase. The depletion is greater and the concentration profile is broader as distance downstream increases.

Figure 4 depicts the sensitivity of predicted silane partial pressure profiles to carrier gas and flow rate. The silane profile in the nitrogen carrier is steeper than in helium, due to the different temperature profile, as discussed above, which results in different decomposition rates. Because the gas-phase temperature is higher in He than in N_2 at a given height above the susceptor, more silane decomposition occurs in He and the silane partial pressure is reduced.

Hydrogen is a product of the SiH_4 decomposition reaction. Thus, an excess of H_2 used as a carrier gas tends to equilibrate the decomposition, resulting in less SiH_4 decomposition. This suppression is reflected in the silane profile in H_2 carrier gas plotted in Fig. 4. At a given temperature, there is much less decomposition of SiH_4 in H_2 than in He. As a result, there is less silane depletion in H_2, and the deposition rate (discussed in the next section) is much less than in He.

Gas velocity has an important effect on the gas-phase concentration profiles. As gas velocity is increased, the residence time of silane in the heated region is reduced. Therefore, when gas-phase kinetics are slow (at low temperatures), the SiH_4 does not react as extensively, and there is less depletion in the silane partial pressure profile. Figure 4 shows this result when the gas velocity is doubled in He carrier gas.

Because H_2 is a product of the silane decomposition, the H_2 concentration profiles are closely related to those of SiH_4. Figure 5 is a plot of hydrogen concentration profiles for a calculation in He carrier. The H_2 concentration increases with distance along the susceptor and is at

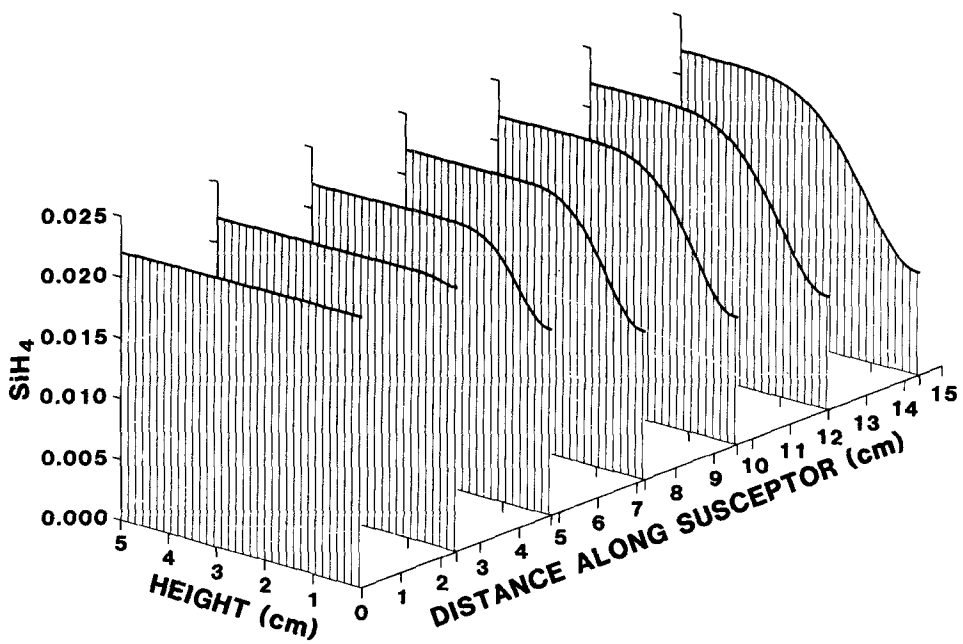

Fig. 3. Silane mass fraction profiles as a function of height above the susceptor and distance along the susceptor for a typical calculation. Input conditions: susceptor temperature = 1000 K, average gas velocity = 12 cm/s, 1.74 torr SiH_4 in 620 torr He.

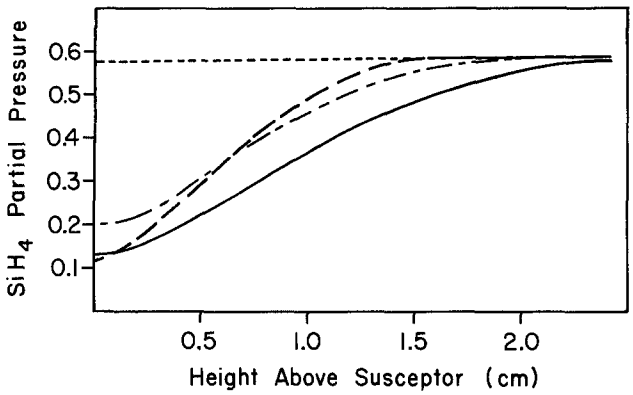

Fig. 4. Silane partial pressure profiles as a function of height above the susceptor, calculated for different carrier gases and initial velocity. Input conditions and identification of curves are the same as in Fig. 2.

maximum near the surface, where silane decomposition is most rapid.

We computed concentration profiles for all chemical species in the reaction scheme (Table I). As an example of the behavior of a typical intermediate species, we plotted profiles of Si_2H_2 in Fig. 6. The Si_2H_2 profile increases with distance along the susceptor as more chemical reactions take place. However, the Si_2H_2 concentration drops to zero at the surface, due to the boundary condition describing deposition (Eq. [9]). Since it has a large gradient at the surface, Si_2H_2 makes a large contribution to the deposition rate in He carrier gas, as we discuss in the next section.

We observed that a reaction zone begins at the leading edge of the susceptor, and it moves outward and downstream as the silane is depleted and heat diffuses out. In this zone chemical production and depletion takes place; outside the zone only transport processes are active. We also observe that the secondary reactions are all equilibrated in the reaction zone. In high temperature cases, even the initiation step equilibrates in the reaction zone. The position of the reaction zone is determined both by heat transfer away from the heated susceptor and mass transfer processes in the gas phase. The process is quite analogous to what occurs in a diffusion flame [see for example, Miller and Kee (26)].

We picture the process as one in which a reaction zone moves away from the susceptor, eating into the unreacted silane. There is a diffusive flux of silane into the reaction zone from the cold region, and there is little diffusive

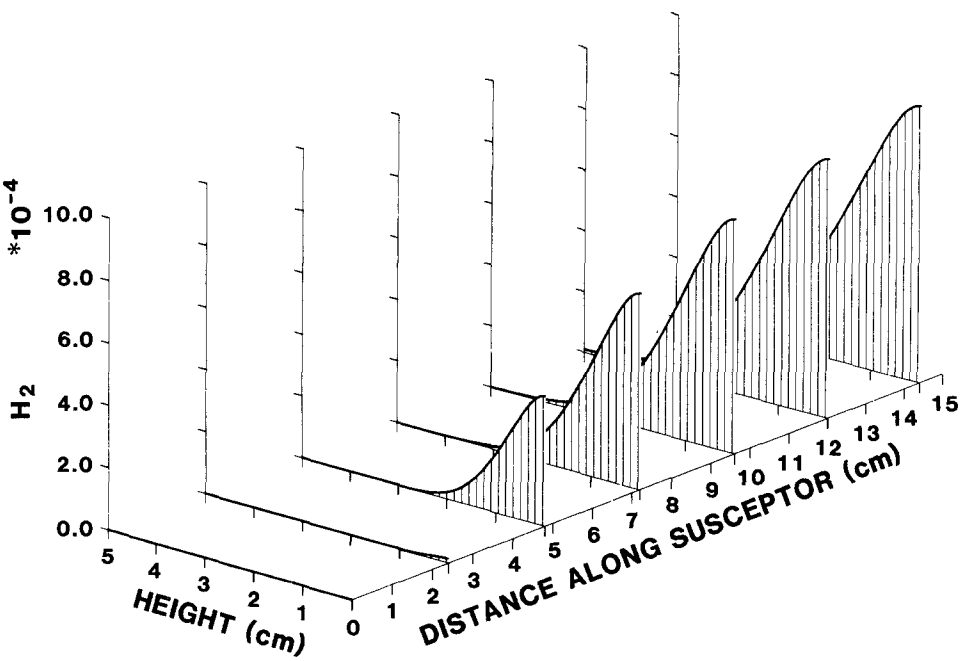

Fig. 5. Hydrogen mass fraction profiles as a function of height above the susceptor and distance along the susceptor. Input conditions are the same as in Fig. 3.

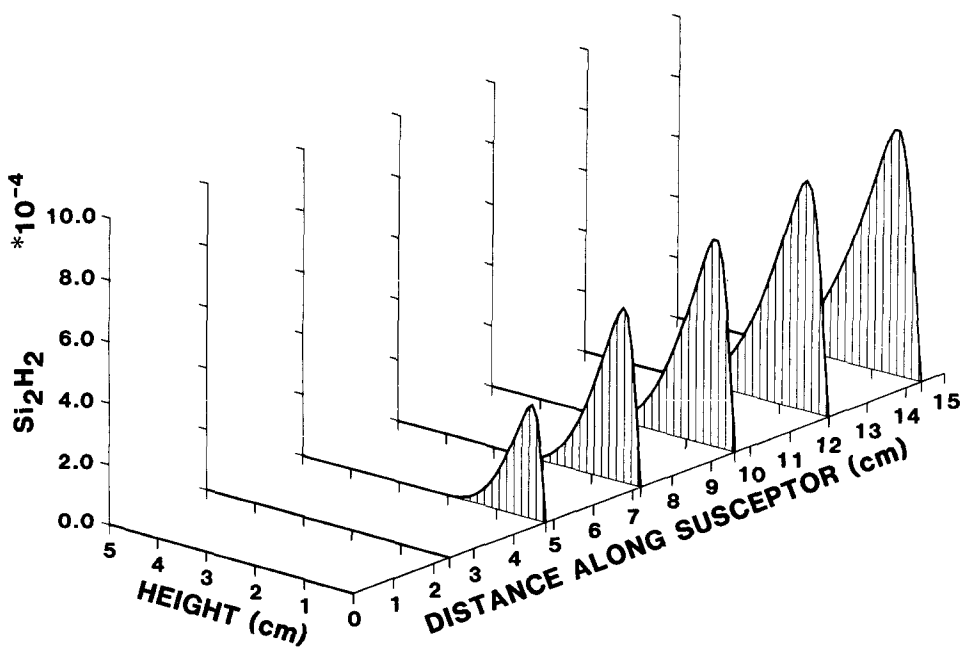

Fig. 6. Si_2H_2 mass fraction profiles as a function of height above the susceptor and distance along the susceptor. Input conditions are the same as in Fig. 3.

flux of silane out of the reaction zone to the susceptor. In high temperature cases, nearly all the silane is depleted in the reaction zone, while in low temperature cases, the silane is not all depleted in the reaction zone because the initiation step is slower. The intermediate species that are chemically produced in the reaction zone diffuse in both directions. The species that diffuse to the susceptor ultimately react on the surface and deposit silicon. The species that diffuse into the cold region remain essentially frozen or unreacted (far from equilibrium) until the reaction zone ultimately reaches them, and reaction occurs.

Within the reaction zone we find a state of "constrained equilibrium" (22). That is, all reactions, except the initiation step, are sufficiently fast that they are essentially in chemical equilibrium. The species production and depletion rates are controlled by diffusive transport and thermodynamic considerations, rather than individual reaction rates. Therefore, we find that the deposition rates and the species profiles are insensitive to the specific rate constants used (except the initiation step). This is fortunate, since there are few measurements of elementary rate constants for the reaction of the silicon intermediate species. However, in many cases the thermodynamic properties that are needed to compute equilibrium constants have been measured, and the others can be estimated from *ab initio* electronic structure computations (12).

Deposition Rate Predictions

A common feature of many CVD systems is that the apparent activation energy for deposition rates at high temperatures is much smaller than at low temperatures. At high temperatures the CVD reactions are very fast. In this case, the deposition rate is limited by the rate at which reactive species can diffuse to the surface, and is not sensitive to temperature. There have been many models for silicon CVD in the high temperature regime (27-46). Usually these models assume that silane does not react in the gas phase, but instead reacts instantaneously at the hot surface. Thus, the SiH_4 concentration at the surface is set to zero as a boundary condition. In many high temperature models, parameters, such as boundary-layer thickness and diffusion constants, are adjusted so that predicted deposition rates match experimental data.

At low temperatures, the apparent activation energy for deposition is much larger than at high temperatures. Because reactions at low temperature are relatively slow, these lower deposition rates have previously been attributed to the kinetics of surface reactions (47-55).

Figure 7 presents a comparison between experimental and theoretical deposition rates as a function of distance along a 1323 K susceptor in H_2 carrier gas. The log of the deposition rate *vs.* distance, from Eversteyn *et al.* (29), was found to be linear, and is represented in Fig. 7 as the solid line. Results of our numerical model are plotted as the square symbols. The agreement between theory and experiment is excellent without adjusting parameters.

At 1323 K, gas-phase decomposition of silane is very fast, and the deposition rate is limited by the rate of diffusion of silicon containing species to the surface. The calculation in Fig. 7 indicates that for these experimental conditions, the radical SiH_2 is primarily responsible for the deposition.

It is useful to compare our model with ones that make the assumptions typically employed in modeling high temperature silicon CVD. These assumptions are that gas-phase decomposition of the SiH_4 does not occur and that SiH_4 reacts instantaneously at the surface, *i.e.*, its concentration is zero there. The results plotted in Fig. 7 as triangles are obtained when our numerical model is used to solve the fluid flow equations with gas-phase chemistry suppressed and the concentration of silane set to zero at the surface, to mimic the previous models. Agreement is very close between the two models, although the mechanisms are dramatically different. This apparent inconsistency is readily explained. The SiH_4 reacts very rapidly in the gas phase close to the susceptor, creating a steep concentration gradient. This silane concentration gradient is nearly equal to that in the second calculation, in which the SiH_4 concentration was set to zero at the surface. In addition, the SiH_2 formed near the surface via reaction R1 diffuses rapidly toward the surface with a diffusion constant close to that of silane. Thus, the rate of diffusion of silicon containing species toward the surface is almost identical in the two calculations.

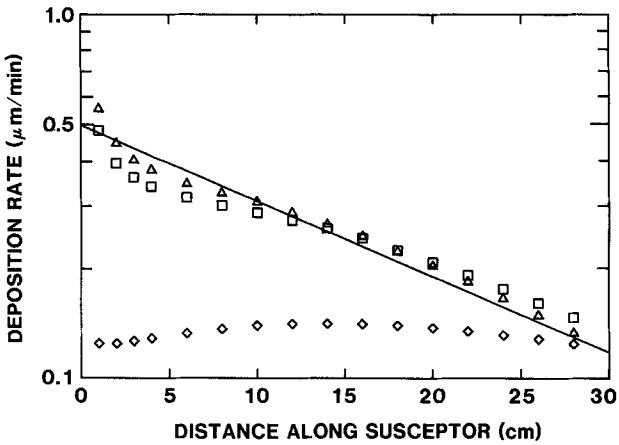

Fig. 7. Comparison of theoretical and experimental deposition rates as a function of distance along the susceptor. Experimental data from Eversteyn et al. (29) is well described by the solid line. Points are from model calculations with the following input conditions: susceptor temperature = 1323 K, average gas velocity = 17.5 cm/s, 0.76 torr SiH_4 in 1 atm of H_2, cell height = 2 cm. Squares are results of the full model. Triangles are results when gas-phase chemistry is omitted and the SiH_4 concentration on the surface is set to zero. Diamonds are results when gas-phase chemistry is omitted and the SiH_4 surface concentration is obtained from Eq. [11].

The assumption that silane reacts with unit probability upon collision with the surface is in variance with experimental results (15, 56-61). Deposition rates calculated when gas-phase chemistry is again suppressed and the surface-reaction probability from Eq. [11] is used as the silane boundary condition are plotted in Fig. 7 as diamonds. This calculation indicates that the measured silane reaction efficiency at the surface is not sufficient to explain the deposition rates of Eversteyn *et al.* (29), and that gas-phase reactions must be included.

Deposition rates predicted by our model as a function of temperature, carrier gas, and total pressure are plotted in Fig. 8. The range of conditions covered in Fig. 8 represents a rigorous test of the model. Experimental deposition rates for a simple cell geometry that can be described well by our two-dimensional model were available only for the case of H_2 carrier gas. The data of van den Brekel (62) are plotted in Fig. 8 as solid triangles. Agreement between experimental and theoretical deposition rates is excellent over the temperature range 700°-1000°C. The model quantitatively predicts the deposition rates, as well as the transition between the high temperature behavior (weak temperature dependence) and low temperature behavior (much higher apparent activation energy). The correct prediction of the low temperature rate is significant because our model includes only the simple surface reaction mechanism described by the boundary conditions, Eq. [9] through [14]. In our model, at low temperatures the apparent activation energy for deposition is principally due to the temperature dependence of the gas-phase reactions in Table I.

The remaining theoretical predictions in Fig. 8 are in qualititive agreement with experimental deposition rate behavior (49, 63, 64). The model predicts two distinct temperature regions, where the apparent activation energies are significantly different. At 1 atm total pressure (APCVD) the low temperature deposition rate in He carrier gas is much higher than in H_2, while at high temperatures they are almost equal. The activation energy is nearly equal in He and H_2 for low temperature APCVD. The knee in the APCVD plot occurs at a temperature 200 degrees higher in H_2 than in He carrier. For the case of 6 torr total pressure (LPCVD) the deposition rate is much greater than for APCVD, and there is very little dependence of deposition rate on carrier gas. The knee in the He curve is shifted to higher temperature as the total pres-

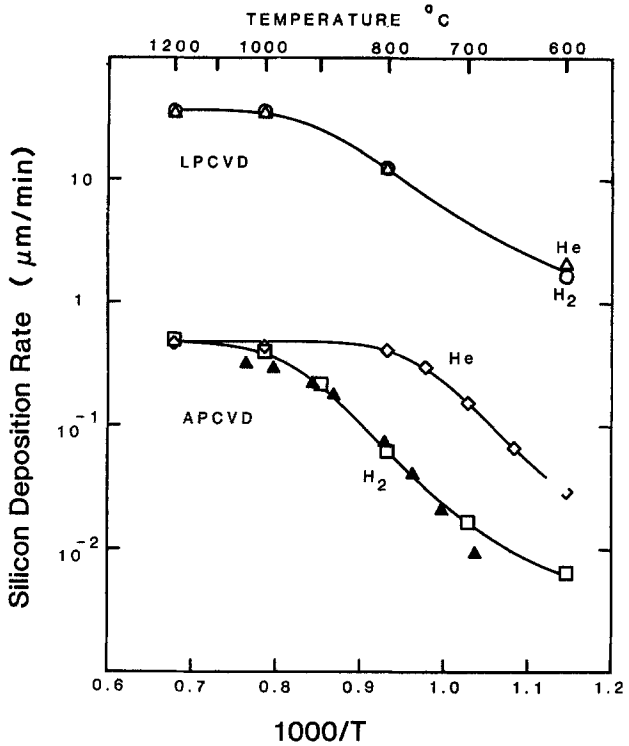

Fig. 8. Deposition rates predicted by the model (open symbols) as a function of temperature, total pressure, and carrier gas. Input conditions for all calculations: average gas velocity = 60 cm/s, 0.76 torr SiH_4 in either 760 torr of carrier gas (APCVD) or 7.6 torr of carrier gas (LPCVD), cell height = 1.25 cm. Deposition rates for APCVD and LPCVD are calculated 15 cm and 1 cm from the leading edge of the susceptor, respectively. Experimental data of van den Brekel (62) is given by the solid triangles. The solid curves have been drawn to distinguish between sets of calculated results.

sure is reduced with the silane partial pressure held fixed.

Many of the reaction rate constants in Table I were estimated. However, all of the calculations represented by Fig. 1-8 were performed with the same set of rate constants, diffusion coefficients, etc. There has been no adjustment of parameters in the model to obtain agreement with experimental CVD data.

The chemical species that contributes most to the deposition process changes with experimental conditions. Figure 9a gives the percent contribution to the deposition rate of the various silicon containing chemical species in H_2 carrier gas, over the temperature range 600°-1200°C. At low temperatures, the silane surface decomposition reaction described by the boundary conditions in Eq. [11] through [13] contributes most to deposition. Below about 700°C, gas-phase reactions are very slow in H_2 carrier gas. Presence of the excess of H_2 inhibits the rate of decomposition by shifting the equilibrium toward the reactants. At higher temperatures, SiH_2 becomes the most important species contributing to deposition. SiH_2 is the product of the first step in the decomposition mechanism of silane. It is assumed to react at the surface with unit probability to form solid silicon and liberate H_2 gas.

Figure 9b is a similar plot for He carrier gas. Gas-phase chemistry is much faster in He than in H_2 and so, even at 600°C, the surface decomposition of SiH_4 is not nearly as important as in H_2 carrier. At temperatures below about 1000°C, Si_2H_2 is the species that contributes most to the deposition rate. Si_2H_2 is formed primarily because of the series of reactions R1,-R4,-R14. Each of these reactions is suppressed in an excess of H_2, which is why Si_2H_2 is unimportant in Fig. 9a. At higher temperatures, Si_2 and Si_3 make the largest contribution to the deposition rate. These chemical species are formed in the reaction sequence R1,-R4,-R14,-R17,-R20, and -R13. This reaction sequence is also suppressed in H_2.

Large concentrations of Si_2 and Si_3 are predicted in the gas phase, close to the susceptor. The model predicts 0.01 torr partial pressure of Si_2 above the susceptor at 1000°C in He carrier gas for the conditions described in Fig. 8. On the basis of these model predictions, Ho and Breiland (65) recently have used laser-excited fluorescence to detect Si_2 above the susceptor in a CVD reactor. This observation of Si_2 is a dramatic confirmation that the gas phase is far from thermodynamic equilibrium [in which Si_2 concentration would be roughly 2×10^{-18} torr, for the conditions of their experiment (65)]. The presence of Si_2 is predicted to turn on very rapidly with temperature, and to be sup-

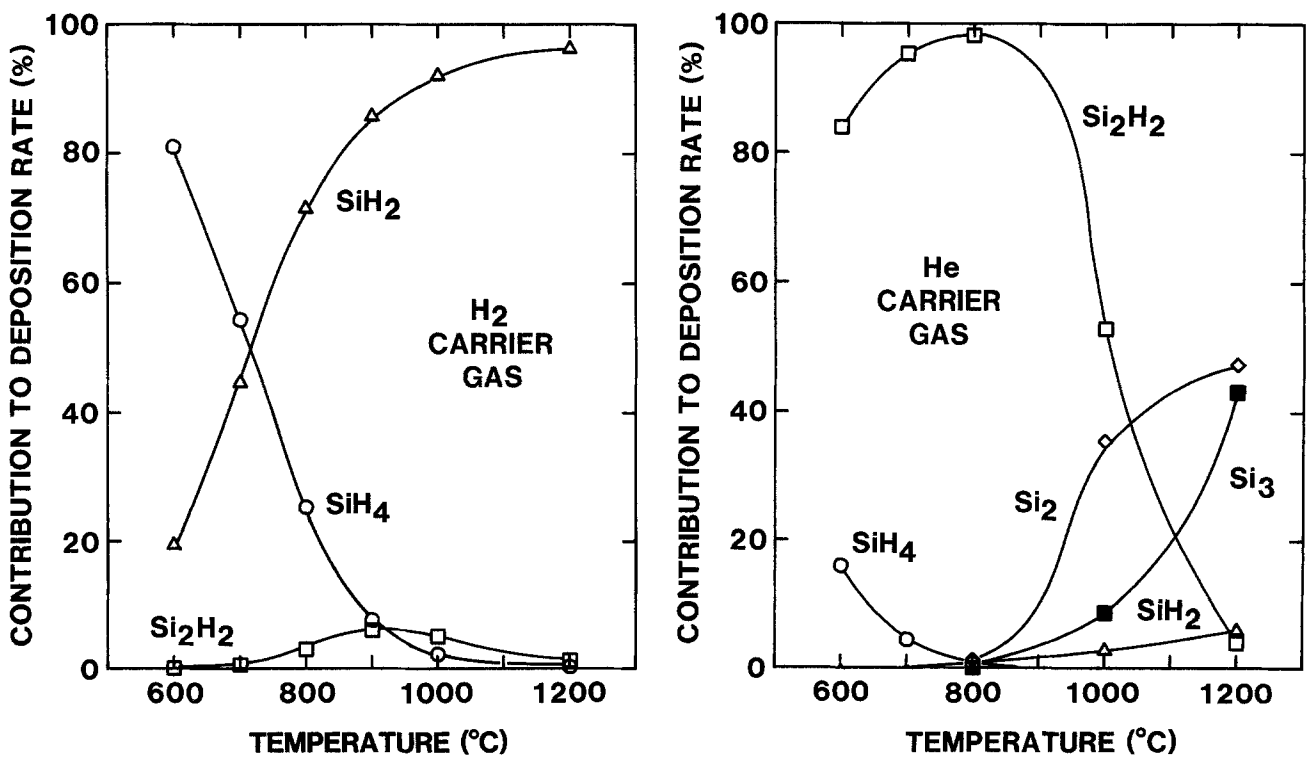

Fig. 9. Percent contributions made to the deposition rate by various chemical species as a function of temperatures in (a, left) H_2 carrier gas, and (b, right) He carrier gas. The chemical species and symbol in each plot are: SiH_4 (open circle), SiH_2 (open triangle), Si_2H_2 (open square), Si_2 (open diamond) and Si_3 (closed square).

pressed by about 5 orders of magnitude in an atmosphere of H_2 carrier. The behavior of the Si_2 and Si_3 concentrations closely mimic experimental observations of gas-phase nucleation of particulates in a CVD reactor. Particulates are observed to form very rapidly above a threshold temperature and are suppressed in H_2 carrier. It is possible that the reaction pathway leading to Si_2 and Si_3 is the precursor to the formation of these nucleation particles.

Summary

We have presented results of a detailed mathematical model of the coupled hydrodynamics and gas-phase chemical kinetics in the CVD of silicon from silane. The model has been used to predict gas-phase temperature, velocity, and chemical species concentration fields. The model also predicts deposition rates as a function of experimental variables, such as susceptor temperature, carrier gas, pressure, and flow velocity. Predicted deposition rates were in excellent agreement with experimental data in Fig. 7 and 8, without use of adjustable parameters.

The model indicates that at high temperatures silane decomposes very rapidly in the gas phase. Radicals formed from this decomposition diffuse to the surface and are primarily responsible for the deposition. The low temperature deposition rate was also described well by our gas-phase kinetics model. The success of the model at low temperature is significant, because the temperature dependence of the deposition rate there has previously been attributed to the rate of reactions on the surface.

These results indicate that the gas phase is very important in silicon CVD. The role of the gas phase merits much more attention than it has previously been given.

Acknowledgments

We would like to thank W. G. Breiland for many helpful discussions about the research presented here. The assistance of L. R. Petzold and J. S. Binkley is also gratefully acknowledged. This work was performed at Sandia National Laboratories and was supported by the U.S. Department of Energy under contract no. DE-AC04-76DP00789 for the Office of Basic Energy Sciences.

Manuscript submitted May 23, 1983; revised manuscript received Sept. 29, 1983. This was Paper 547 RNP presented at the Minneapolis, Minnesota, Meeting of the Society, May 10-15, 1981.

Sandia National Laboratories assisted in meeting the publication costs of this article.

REFERENCES

1. M. C. Branch, R. J. Kee, and J. A. Miller, *Combust. Sci. Tech.*, **29,** 147 (1982).
2. J. A. Miller, R. E. Mitchell, M. D. Smooke, and R. J. Kee, 19th International Symposium on Combustion, Pittsburgh, p. 181 (1982).
3. P. Ho and W. G. Breiland, *Appl. Phys. Lett.*, **43,** 125 (1983).
4. See, for example, "Theory of Laminar Flows," Vol. IV, High Speed Aerodynamics and Jet Propulsion," F. K. Moore, Editor, Princeton University Press, Princeton, NJ (1964).
5. R. A. Svehla, NASA Technical Report R-132 (1962).
6. C. F. Curtiss and J. O. Hirschfelder, *J. Chem. Phys.*, **17,** 550 (1949).
7. C. R. Wilke, *ibid.* **18,** 517 (1950).
8. J. O. Hirschfelder, C. F. Curtiss, and R. B. Bird, "Molecular Theory of Gases and Liquids," John Wiley and Sons, New York (1954).
9. R. J. Kee and J. A. Miller, Sandia National Laboratories Report, SAND 81-8241 (1981).
10. "JANAF Thermochemical Tables," Dow Chemical Company, (1965), and subsequent addenda.
11. S. Gordon and B. J. McBride, NASA SP-273 (1971).
12. J. S. Binkley, Unpublished.
13. S. W. Benson, "Thermochemical Kinetics," 2nd ed., John Wiley and Sons, New York (1976).
14. R. J. Kee, J. A. Miller, and T. H. Jefferson, Sandia National Laboratories Report, SAND 80-8003 (1980).
15. R. F. C. Farrow, *This Journal*, **121,** 899 (1974).
16. H. E. O'Neal, Personal communication. The Arrhenius factors are from an RRKM analysis of data described in (17).
17. C. G. Newman, H. E. O'Neal, M. A. Ring, F. Leska, and N. Shipley, *Int. J. Chem. Kinet*, **11,** 1167 (1979).
18. P. John and J. H. Purnell, *J. Chem. Soc*, **69,** 1455 (1973).
19. E. R. Austin and F. W. Lampe, *J. Phys. Chem.*, **81,** 1134 (1977).
20. J. A. Confer, K. P. Lynch, and J. V. Michael, *ibid.* **79,** 1139 (1975).
21. M. E. Coltrin and J. S. Binkley, Unpublished.
22. J. C. Keck, in "Maximum Entropy Formalism," R. D. Levine and M. Tribus, Editors, MIT Press, Cambridge, MA (1978).
23. M. A. Kramer, R. J. Kee, and H. Rabitz, Sandia National Laboratories Report, SAND82-8230 (1982).
24. L. R. Petzold, Sandia National Laboratories Report, SAND 82-8637 (1982).
25. C. W. Gear, "Numerical Initial Value Problems in Ordinary Differential Equations," Prentice-Hall, Englewood Cliffs, NJ (1971).
26. J. A. Miller and R. J. Kee, *J. Phys. Chem.*, **81,** 2534 (1977).
27. S. E. Bradshaw, *Int. J. Electron.* **21,** 205 (1966).
28. S. E. Bradshaw, *ibid.* **23,** 381 (1967).
29. F. C. Eversteyn, P. J. W. Severin, C. H. J. van den Brekel, and H. L. Peek, *This Journal*, **117,** 925 (1970).
30. F. C. Eversteyn and H. L. Peek, Philips Res. Rep., **25,** 472 (1970).
31. F. C. Eversteyn, *ibid.* **29,** 45 (1974).
32. J. Bloem, This Journal, **117,** 1397 (1970).
33. P. van der Putte, L. J. Giling, and J. Bloem, *J. Cryst. Growth*, **31,** 299 (1975).
34. S. Berkman, V. S. Ban, and N. Goldsmith in "Heteroepitaxial Semiconductor Electronic Devices," G. W. Cullen and C. C. Wang, Editors, Chap. 7, Springer, New York (1978).
35. W. H. Shepherd, *This Journal*, **112,** 988 (1965).
36. R. W. Andrews, D. M. Rynne, and E. G. Wright, *Solid State Technol*, 61 (Oct. 1969).
37. P. C. Rundle, *Int. J. Electron.*, **24,** 405 (1968).
38. P. C. Rundle, *J. Cryst. Growth*, **11,** 6 (1971).
39. R. Takahashi, K. Sugawara, Y. Nakazawa, and Y. Koga, in "Chemical Vapor Deposition," J. M. Blocher and J. C. Withers, Editors, p. 695, The Electrochemical Society Softbound Proceedings Series, New York (1970).
40. K. Sugawara, H. Tochikubo, R. Takahashi, and Y. Koga, *ibid.*, p. 713.
41. R. Takahashi, Y. Koga, and K. Sugawara, *This Journal*, **119,** 1406 (1972).
42. K. Sugawara, *ibid.*, **119,** 1749 (1972).
43. E. Fujii, H. Nakamura, K. Haruna, and Y. Koga, *ibid.*, **119,** 1106 (1972).
44. C. W. Manke and L. F. Donaghey, in "Chemical Vapor Deposition," L. F. Donaghey, P. Rai-Choudhury, and R. N. Tauber, Editors, p. 151, The Electrochemical Society Softbound Proceedings Series, Princeton, NJ (1977).
45. C. W. Manke and L. F. Donaghey, *This Journal*, **124,** 561 (1977).
46. M. L. Hitchman, *J. Cryst. Growth*, **48,** 394 (1980).
47. B. A. Joyce and R. R. Bradley, *This Journal*, **110,** 1235 (1963).
48. M. J. Duchemin, M. M. Bonnet, and M. F. Koelsch, *ibid.*, **125,** 637 (1978).
49. J. Bloem and L. J. Giling, in "Current Topics in Materials Science," E. Kaldis, Editor, Chap. 4, North-Holland (1978).
50. M. L. Hitchman, in "Chemical Vapor Deposition," T. O. Sedgwick and H. Lydtin, Editors, p. 59, The Electrochemical Society Softbound Proceedings Series, Princeton, NJ (1979).
51. M. L. Hitchman, J. Kane, and A. E. Widmer, *Thin Solid Films*, **59,** 231 (1979).
52. F. Hottier and R. Cadoret, *J. Cryst. Growth*, **52,** 199 (1981).
53. J. Holleman and T. Aarnink, in "Chemical Vapor Deposition," J. M. Blocher, G. E. Vuillard, and G. Wahl, Editors, p. 307, The Electrochemical Society Softbound Proceedings Series, Pennington, NJ (1981).
54. W. A. P. Claassen and J. Bloem, *J. Cryst. Growth*, **51,** 443 (1981).
55. W. A. P. Claassen, J. Bloem, W. G. J. N. Valkenburg, and C. H. J. van den Brekel, *ibid.* **57,** 259 (1982).
56. B. A. Joyce and R. R. Bradley, *Philos. Mag.*, **14,** 289 (1966).
57. G. R. Booker and R. R. Bradley, *ibid.*, **14,** 301 (1966).
58. B. A. Joyce, R. R. Bradley, and G. R. Booker, *ibid.*, **15,** 1167 (1967).
59. B. E. Watts, R. R. Bradley, B. A. Joyce, and G. R. Booker, *ibid.*, **17,** 1163 (1967).
60. B. A. Joyce, R. R. Bradley, B. E. Watts, and G. R.

Booker, *ibid.*, **19,** 403 (1968).
61. R. C. Henderson and R. F. Helm, *Surf. Sci.*, **30,** 310 (1972).
62. C. H. J. van den Brekel, Ph.D. Thesis, University of Nijmegen, The Netherlands (1978).
63. W. A. P. Claassen and J. Bloem, *Philips J. Res.*, **36,** 122 (1981).
64. W. A. Bryant, *Thin Solid Films*, **60,** 19 (1979).
65. P. Ho and W. G. Breiland, *Appl. Phys. Lett.*, To be published.

Controlled Reactive Sputter Synthesis of Refractory Oxides

SiO_x, The Silicon-Oxygen System

Troy W. Barbee, Jr., Douglas L. Keith, Lynn Nagel, and William A. Tiller

Department of Materials Science and Engineering, Stanford University, Stanford, California 94305

ABSTRACT

Reactive sputter deposition of refractory oxides, under conditions in which the reaction between the sputtered species and the oxygen is isolated to the deposition surface, has been experimentally investigated, and results have been obtained for the formation of SiO_x ($0 < x < 2$). It is shown that the dependence of the deposited film stoichiometry on oxygen pressure and the incidence rate of silicon can be correlated with reported results of oxygen adsorption onto single-crystal silicon surfaces and amorphous silicon surfaces. This correlation is made in terms of oxygen exposure and, in our work, a dynamic exposure (L_D) is defined for steady-state synthesis conditions by placing the origin of a moving reference frame at the deposition surface. This correlation shows that the sticking coefficient of oxygen onto room temperature substrates is independent of oxygen coverage (*i.e.*, surface stoichiometry) for coverages less than 0.8. This requires that a mobile precursor adsorption process be operative for oxygen in our experiments. The deduced pressure-independent oxygen sticking coefficient is 1.5 to 4.1 $\times 10^{-3}$.

Sputter deposition of refractory compound films of high quality from compound targets is difficult because of the low mechanical integrity of such targets, their low thermal conductivities, inherently low deposition rates, poor stoichiometry control, and the often substantial contamination incurred during the sputter target preparation (1-5). These difficulties may be diminished by reactive sputtering in which the target, consisting of the metal component, is sputtered using a gas mixture consisting of an inert gas (typically argon) and a reactive component, one element of which is active in the formation of the desired compound (1, 2, 6-11). Despite present drawbacks, associated with the difficulty of closely controlling film stoichiometry, reactive sputtering often yields much higher quality films at deposition rates somewhat higher than those attained using compound targets.

The purpose of the work presented in this paper was to develop the reactive sputtering synthesis process so that continuous layers of controllable structure and composition could be formed in a reproducible and routine manner. In this paper we report the results of our studies on the reactive deposition of the oxides of silicon (SiO_x). Films of SiO_x ($0 \leq x \leq 2$) were synthesized at high rates onto substrates held at room temperature. A systematic investigation of the structure-composition-synthesis process variables was conducted for this system, and it was clearly demonstrated that films of controllable stoichiometry, varying over the range $SiO_{0.1}$ to SiO_2, can be reproducibly synthesized at rates (>5 Å/s) equal to or greater than those typically encountered in industry. In addition, the substrate temperature during synthesis was held close to the ambient condition ($T_s \leq 65$°C). The low temperature nature of this process is a unique feature of high industrial potential, as it provides a method for forming SiO_x passivating films that does not include time-temperature cycling which could degrade existing device structures.

Experimental Approach and Procedures

The experimental approach was to design experiments so that reaction between the sputtered species (Si in this case) and the reactive gas (O_2) was forced to occur at the deposition surface. It was believed that under such conditions, high deposition rates plus control of structure and stoichiometry would be attainable through control of the relative rates of incidence of the two reactive components onto this surface. Additionally, if such control were possible, it would facilitate both modeling of the reactive sputtering process and experimental reproducibility in both a given laboratory and between laboratories.

Key words: sputtering, refractories, deposition.

The experimental arrangement (type II) used was designed to isolate the sputter-source plate from the oxygen gas, maintaining it in an inert argon gas atmosphere while introducing an oxygen pressure at the substrate. Two approaches were taken here. In the first (type IIA), argon and oxygen were brought into the chamber separately, with the oxygen inlet surrounding the substrate and the argon introduced as under normal sputtering conditions. In these experiments, the oxygen, though localized at the substrate, was nonuniformly distributed. Also, although higher oxygen concentrations were attainable, source contamination by oxygen still limited the experimental range. A series of experiments was performed using this apparatus, in which the rate of incidence of silicon was held constant and the oxygen pressure at the substrate varied. In this work, the source to substrate distance was 11.5 cm and (100) single-crystal silicon wafers were used as substrates. The silicon incidence rate was 2.9 Å/s (1.45 $\times 10^{15}$ Si atoms/cm^{2}s). Oxygen incidence rates were varied from 0 to 8 $\times 10^{17}$ O_2/cm^{2}s ($0 \leq P_{O_2} \leq 1.6$ mtorr).

A second-generation apparatus (type IIB) was designed so that the range of oxygen pressures could be extended and the distribution of oxygen at the deposition surface would be uniform. Two gas ring sources, one for argon and the other for oxygen, were fabricated with the gas inlets in each ring consisting of slits 0.002 in. wide on the inner diameter of two-piece annular structures. For oxygen, the sample was mounted in the ring with the oxygen directed down onto the substrate. For argon, the ring was mounted near the sputter source with the argon stream directed at the sputter-source target. This arrangement is schematically shown in Fig. 1. Improved film uniformity both in thickness and composition was attained with this apparatus. Additionally, oxygen pressures approximately twice those accessible without the argon isolation ring were usable without oxidation of the silicon source plate in the magnetron sputter head. For these experiments, silicon incidence rates were 3.4, 5.9, and 8.2 Å/s or 1.72 $\times 10^{15}$ Si/cm^{2}s, 2.9 $\times 10^{15}$ Si/cm^{2}s and 4.1 $\times 10^{15}$ Si/cm^{2}s, respectively. The general oxygen pressure varied from 0 to 0.6 mtorr (0.08 Pa) in the system. This is considerably lower than the oxygen pressure at the substrate, which was not locally measured in these experiments.